

CARBON MONOXIDE OBSERVATIONS TOWARD STAR FORMING REGIONS IN THE OUTER SCUTUM-CENTAURUS SPIRAL ARM

TREY V. WENGER,^{1,2} ASAD A. KHAN,¹ NICHOLAS G. FERRARO,¹ DANA S. BALSER,² W. P. ARMENTROUT,^{3,4}
L. D. ANDERSON,^{3,5,4} AND T. M. BANIA⁶

¹*Astronomy Department, University of Virginia, P.O. Box 400325, Charlottesville, VA 22904-4325, USA.*

²*National Radio Astronomy Observatory, 520 Edgemont Rd., Charlottesville, VA 22903, USA.*

³*Department of Physics and Astronomy, West Virginia University, PO Box 6315, Morgantown WV 26506, USA.*

⁴*Center for Gravitational Waves and Cosmology, West Virginia University, Chestnut Ridge Research Building, Morgantown, WV 26505, USA.*

⁵*Adjunct Astronomer at the Green Bank Observatory, P.O. Box 2, Green Bank WV 24944, USA.*

⁶*Institute for Astrophysical Research, Department of Astronomy, Boston University, 725 Commonwealth Avenue, Boston, MA, 02215, USA.*

(Revised May 10, 2022 Submitted – TVW)

ABSTRACT

The Outer Scutum-Centaurus arm (OSC) is the most distant molecular spiral arm known in the Milky Way. The OSC may be the very distant end of the well-known Scutum-Centaurus arm, which stretches from the end of the Galactic bar to the outer Galaxy. At this distance the OSC is seen in the first Galactic quadrant. The population of star formation tracers in the OSC remains largely uncharacterized. Extragalactic studies show a strong correlation between molecular gas and star formation, and carbon monoxide (CO) emission was recently discovered in the OSC. Here we use the Arizona Radio Observatory (ARO) 12 m telescope to observe the ¹²CO J = 1–0 and ¹³CO J = 1–0 transitions toward 78 H II region candidates chosen from the *WISE* Catalog of Galactic H II Regions. These targets are spatially coincident with the Galactic longitude-latitude (ℓ, b) OSC locus as defined by H I emission. We detect CO emission in $\sim 80\%$ of our targets. In total, we detect 117 ¹²CO and 40 ¹³CO emission lines. About 2/3 of our targets have at least one emission line originating beyond the Solar orbit. Most of the detections beyond the Solar orbit are associated with the Outer Arm, but there are 17 ¹²CO emission lines and 8 ¹³CO emission lines with LSR velocities that are consistent with the velocities of the OSC. There is no apparent difference between the physical properties (e.g., molecular column density) of these OSC molecular clouds and non-OSC molecular clouds within our sample.

Keywords: Galaxy: structure, ISM: molecules, radio lines: ISM, surveys

1. INTRODUCTION

Galactic structure in the Milky Way is difficult to determine because of our location within the disk and the difficulties in deriving accurate distances. There is strong evidence, however, that the Milky Way is a barred spiral galaxy (e.g., Churchwell et al. 2009). Most barred spiral galaxies are Grand Design galaxies, with two prominent symmetric spiral arms (Elmegreen & Elmegreen 1982). Understanding the Milky Way structure is important since bars and spiral arms have dynamical effects (e.g., radial migration) and influence star formation (e.g., shock gas).

To our knowledge, Dame & Thaddeus (2011) were the first to connect the Scutum-Centaurus (SC) spiral arm from its beginning at the end of the bar in the inner Galaxy to the outer Galaxy in the first quadrant. They called this outermost section the Outer Scutum-Centaurus (OSC) arm. In the first quadrant, the OSC is at a distance between 15 kpc and 19 kpc from the Galactic Center (GC) and between 20 kpc and 25 kpc from the Sun (Armentrout et al. 2017). The connection between the SC and OSC arm segments, however, remains hypothetical. Toward the GC, velocity crowding and complex structure prohibits clear identification of spiral structure. The HI emission that has now been associated with the OSC arm was detected long ago. The arm appears in the early 21 cm maps of both Kerr (1969) and Weaver (1974). Yet it took decades to trace the SC spiral arm from the bar to the outer Galaxy.

Dame & Thaddeus (2011) carefully traced the OSC in the Leiden/Argentine/Bonn (LAB) HI 21 cm line all-sky survey data (Hartmann & Burton 1997; Arnal et al. 2000; Bajaja et al. 2005; Kalberla et al. 2005) and then, using the Center for Astrophysics 1.2 m telescope, detected molecular gas in the arm for the first time, at 10 locations coincident with HI emission peaks. A CO map was made of one location revealing a molecular cloud with mass and radius of $5 \times 10^4 M_{\odot}$ and 47 pc, respectively. Koo et al. (2017) recently re-analyzed the LAB survey data using a peak-finding algorithm and identified the OSC arm as a 20 kpc long HI structure coincident with several HII regions and molecular clouds.

Sun et al. (2015) suggested a possible extension of the OSC from the first Galactic quadrant into the second quadrant. Their results are part of the Milky Way Imaging Scroll Painting (MWISP) project to map ^{12}CO and ^{13}CO from Galactic longitudes $-10^{\circ} < \ell < 250^{\circ}$ and Galactic latitudes $-5^{\circ} < b < 5^{\circ}$ with the Purple Mountain Observatory Delingha 13.7 m telescope. They detected 72 molecular clouds with masses between $10^2 - 10^4 M_{\odot}$ that lie between $120^{\circ} < \ell < 150^{\circ}$ and are roughly consistent with an extension of the OSC as-

suming a log-periodic spiral arm model. First quadrant data from the MWISP for the longitude range of $35^{\circ} < \ell < 45^{\circ}$ reveal 168 molecular clouds consistent with the OSC (ℓ, v) locus, defined by $V_{\text{LSR}} = -1.6 \ell \pm 13.2 \text{ km s}^{-1}$. These molecular clouds have typical masses and sizes of $3 \times 10^3 M_{\odot}$ and 5 pc, respectively (Sun et al. 2017).

Detection of CO does not necessarily imply star formation. Observations of high-mass star formation tracers are therefore critical for characterizing the OSC. HII regions are the archetypical tracers of star formation and spiral structure. As part of the HII Region Discovery Survey, Anderson et al. (2015) discovered six HII regions whose radio recombination line (RRL) emission velocities are consistent with the OSC (ℓ, v) locus defined by $V_{\text{LSR}} = -1.6 \ell \pm 15 \text{ km s}^{-1}$. There are four additional HII regions in the WISE Catalog of Galactic HII Regions consistent with this definition of the OSC (Anderson et al. 2012).

RRL emission is the best tracer of high-mass star formation, but it is faint at the large distances of the OSC. Armentrout et al. (2017) took a different approach and used the Green Bank Telescope (GBT) to observe the dense molecular gas tracers NH_3 (J,K) = (1,1), (2,2), (3,3) and H_2O 6(1,6) \rightarrow 5(2,3) toward 75 WISE HII regions and HII region candidates located within the OSC (ℓ, b) locus as defined by HI (Dame & Thaddeus 2011). Because these targets were identified as HII region candidates based on their mid-infrared morphology, these molecular lines trace dense gas that is more likely to be associated with star formation. Any detected spectral line *probably* indicates an active star formation region. About 20% of the targets were detected in either ammonia or water maser emission, but only two have velocities consistent with the OSC.

Armentrout et al. (2017) also observed a similar sample of OSC targets in radio continuum at 8–10 GHz with the Jansky Very Large Array (JVLA). About 60% of the targets were detected in radio continuum with the JVLA. Five of these are associated with the locus of the OSC. Together, RRL and continuum emission allowed various HII region physical properties to be derived. Associating the radio continuum with the molecular transition, however, is less secure since the molecular cloud may not be associated with the HII region (Anderson et al. 2009). Nonetheless, assuming they are related yields a distance. If the hydrogen-ionizing photon flux is produced by a single star, then the observed radio continuum fluxes imply spectral types ranging from O4 to O8.5. This suggests that even at such large Galactocentric distances (> 15 kpc) high-mass star formation is ongoing in the Milky Way.

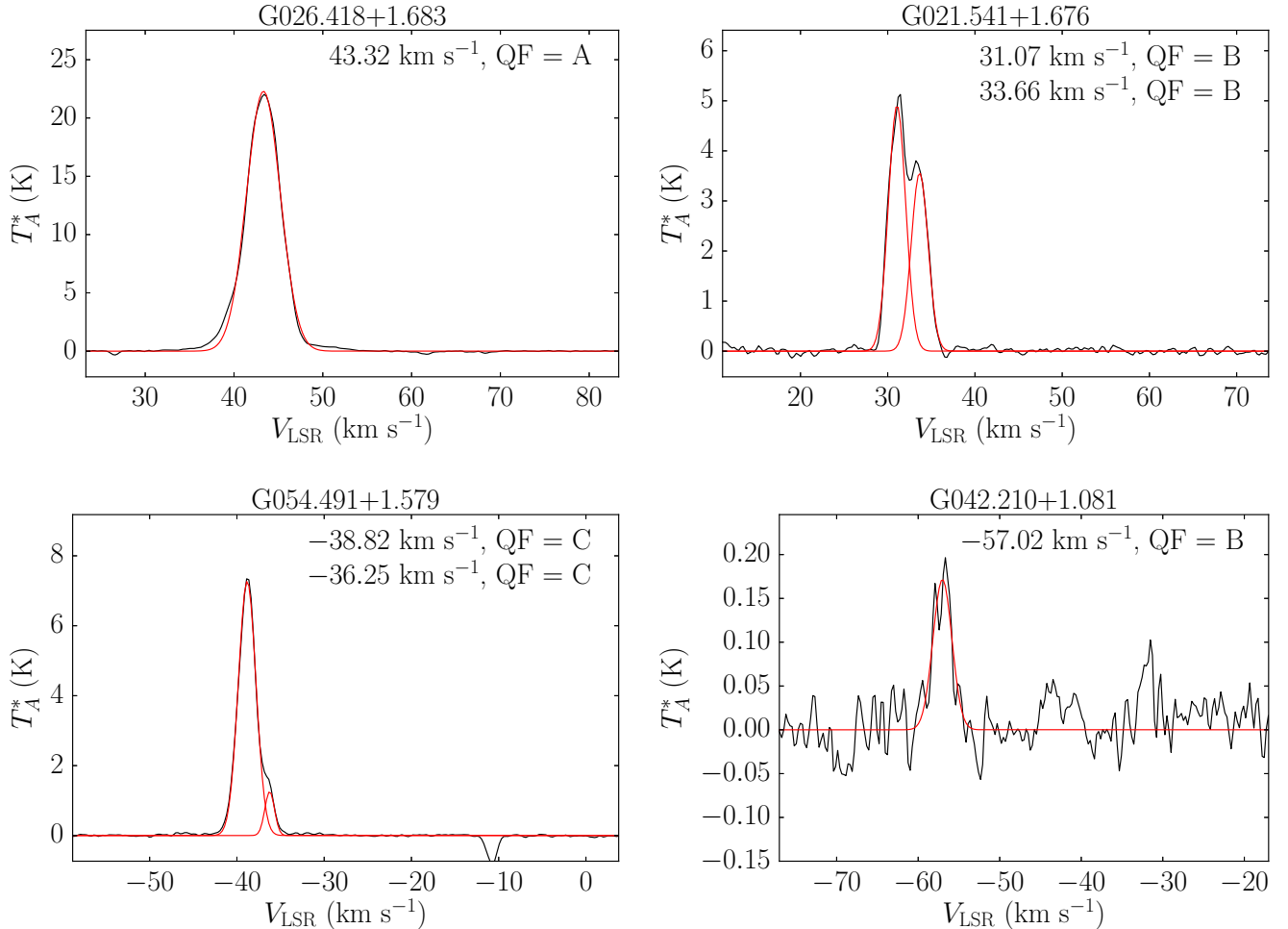


Figure 1. Representative ^{12}CO spectra for different quality factors (QF). Plotted is the antenna temperature as a function of the LSR velocity. The black curves are the data and the red curves are Gaussian fits to the data. The LSR velocity of each Gaussian profile, together with the QF, is shown in the right-hand corner of the plot.

Here we seek to explore the molecular content in the OSC using ^{12}CO and ^{13}CO transitions, which are brighter than the molecular line transitions observed by Armentrout et al. (2017). Since molecular clouds need not be forming high-mass stars, carbon monoxide is not as good a tracer of high-mass star formation as RRLs, NH_3 , or H_2O , but detection is much more likely at these large distances. Following Armentrout et al. (2017) we only target H II regions and H II region candidates from the *WISE* Catalog of Galactic H II Regions. These targets all have the same characteristic infrared morphology which increases the probability that the molecular gas is associated with high-mass star formation.

2. OBSERVATIONS AND DATA REDUCTION

We used the Arizona Radio Observatory (ARO) 12 m telescope to observe the ^{12}CO J=1–0 transition at 115.27120 GHz toward 78 H II regions and H II region candidates located in the first Galactic quadrant. We

selected all H II region candidates in the *WISE* Catalog of Galactic H II Regions (Anderson et al. 2012) that lay near the OSC (ℓ, b) locus defined as $b = 0.375^\circ + 0.075^\circ \times \ell$ within the range $20^\circ < \ell < 70^\circ$. Many of these targets have measured radio continuum emission and are most likely bona fide H II regions (Armentrout et al. 2017). In addition, we included 10 H II regions from (Armentrout et al. 2017) with RRL velocities within the OSC (ℓ, V) locus defined as $V_{\text{LSR}} = -1.6 \ell \pm 15 \text{ km s}^{-1}$. Since ^{12}CO is often optically thick in Galactic molecular clouds, we observed the optically thin ^{13}CO J=1–0 transition at 110.20132 GHz in a subset of targets with bright ^{12}CO detections to provide a more accurate measure of the molecular column density.

The ARO 12 m telescope is the European ALMA prototype antenna that began operation on Kitt Peak in 2014. The telescope’s half-power beam-width (HPBW) is $54''$ and $57''$ at 115 GHz and 110 GHz, respectively.

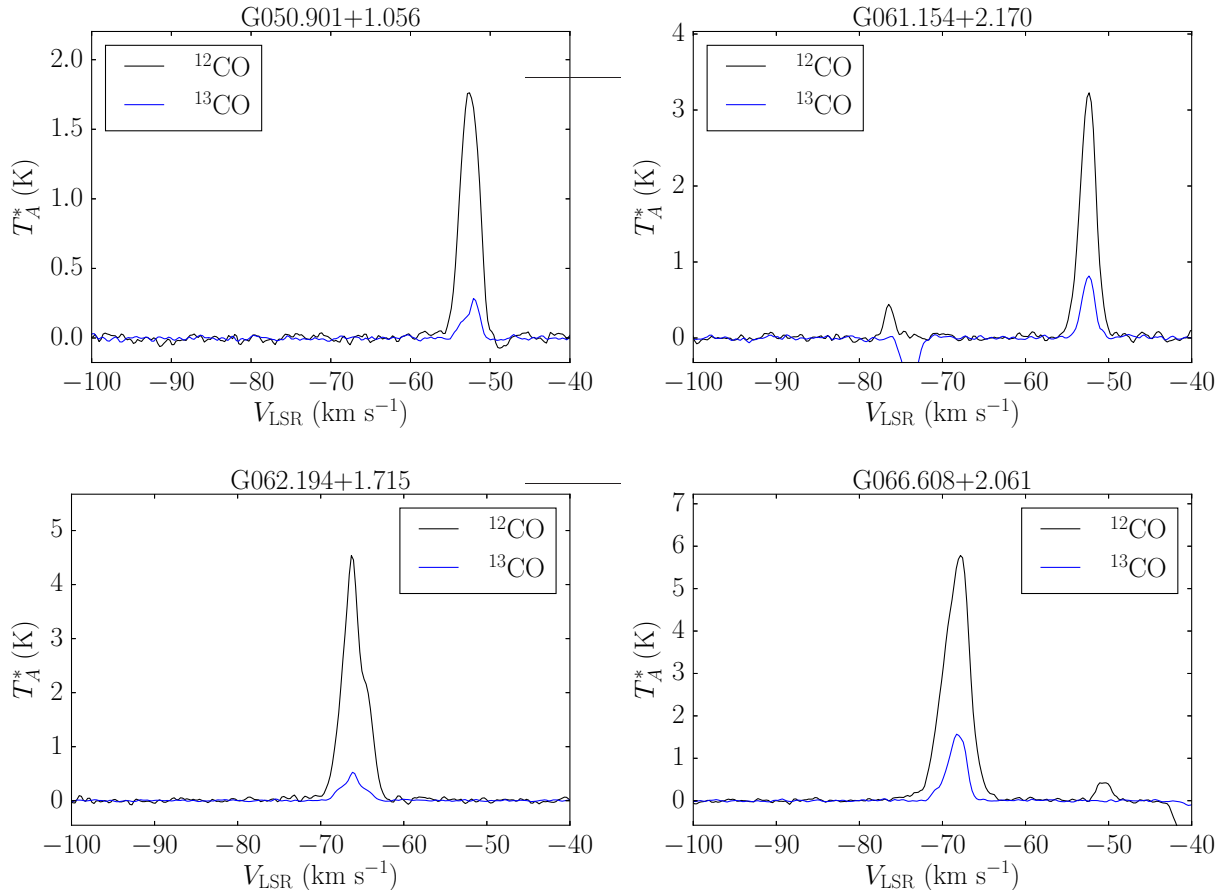


Figure 2. ^{12}CO (black) and ^{13}CO (blue) spectra of targets where the association of ^{12}CO emission and ^{13}CO emission was not straightforward. In G050.901+1.056 and G062.194+1.715 there are two ^{13}CO components that correspond to one ^{12}CO component. In G066.608+2.061 there is one ^{13}CO component that corresponds to two ^{12}CO components. Finally, in G061.154+2.170 there are ^{12}CO components at velocities where the ^{13}CO emission is corrupted by emission in the Off position.

The main beam efficiency is $\gtrsim 90\%$ at these frequencies. Our observations were performed between February 11–16, 2016. The receiver consisted of the ALMA band 3, dual polarization, sideband-separating mixers with typical on-sky system temperatures of ~ 300 K. We employed both the filter bank spectrometer with 256 channels at 2 MHz spectral resolution (5 km s^{-1} at 115 GHz), and the millimeter autocorrelator (MAC) with 4096 channels at 195 kHz spectral resolution (0.5 km s^{-1} at 115 GHz). Both spectrometers accept two intermediate frequency signals consisting of the two orthogonal polarizations. Here we only consider data from the MAC spectrometer given the narrow line widths of CO ($\sim 1 \text{ km s}^{-1}$). The typical atmospheric optical depth at zenith was $\tau_0 \sim 0.2$.

We made total power, position switched observations where the reference position (Off) is offset by $20'$ in azimuth from the source (On). The On and Off positions were observed for 5 minutes each with a switching rate of 30 seconds, for a total time of 10 minutes. Typically 1–2

total power pairs were sufficient to detect ^{12}CO emission but in some cases we integrated longer. The telescope pointing and focus were corrected every 1–2 hours by peaking on Jupiter, Venus, or Saturn. The typical pointing accuracy was $\sim 2''$ rms. At the start of each session we checked the tuning of the spectrometers by observing the test source M17SW.

The data were reduced and analyzed using TM-BIDL, an IDL single-dish software package (Bania et al. 2016).¹ The data reduction and analysis were performed independently by three of the authors. Each spectrum was visually inspected. We discarded $\sim 1\%$ of the spectra due to poor baseline structure. For each target the data were averaged over all total power pairs and polarizations to produce a single, averaged spectrum. We modeled the spectral baselines with a third-order polynomial function that was subtracted from the data to

¹ V7.1, see <https://github.com/tvwenger/tmbidl>

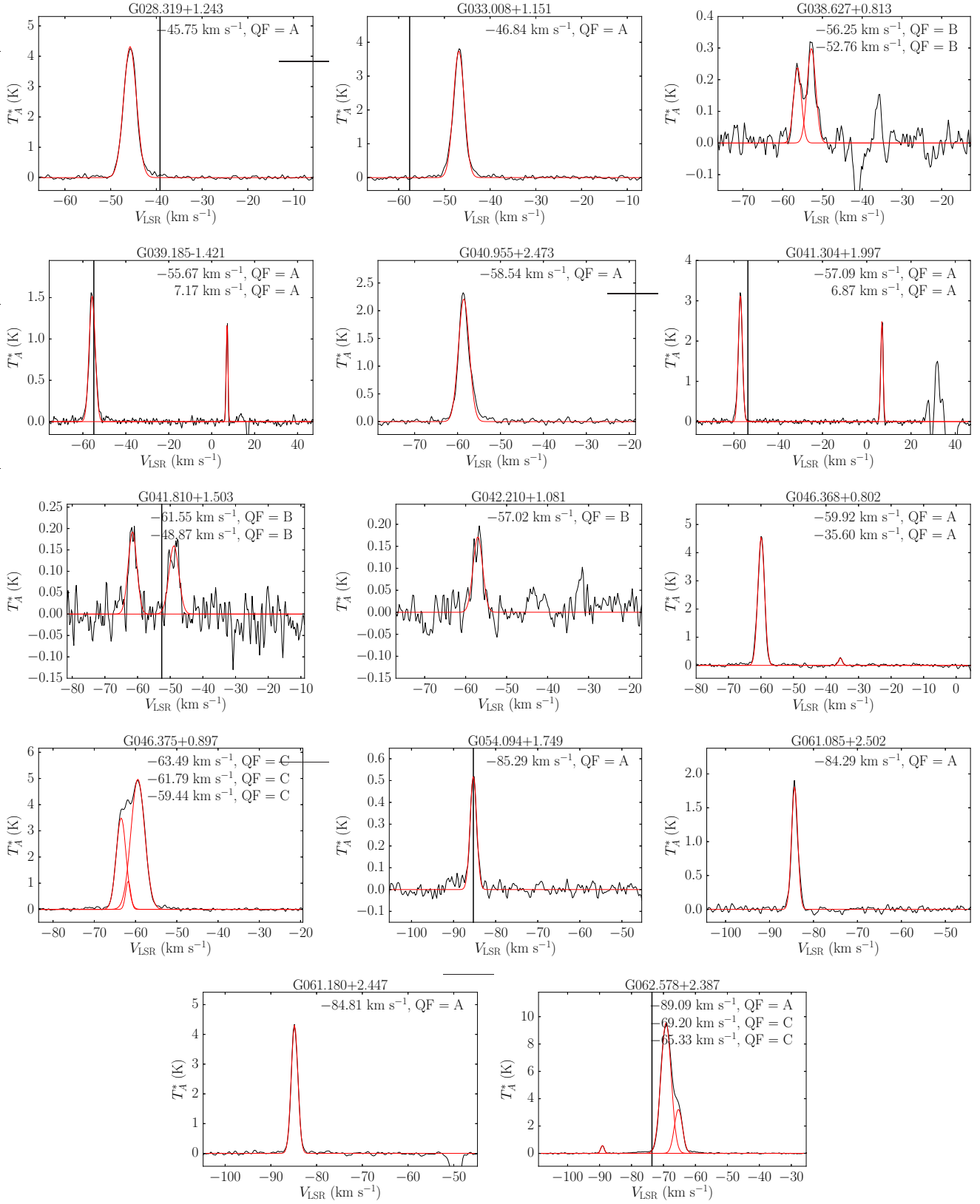


Figure 3. ^{12}CO spectra of emission lines originating within the OSC. Plotted is the antenna temperature as a function of the LSR velocity. The black curves are the data and the red curves are Gaussian fits to the data. The LSR velocity of each Gaussian profile, together with the QF, is shown in the right-hand corner of the plot. The vertical black line indicates the RRL velocity, when available.

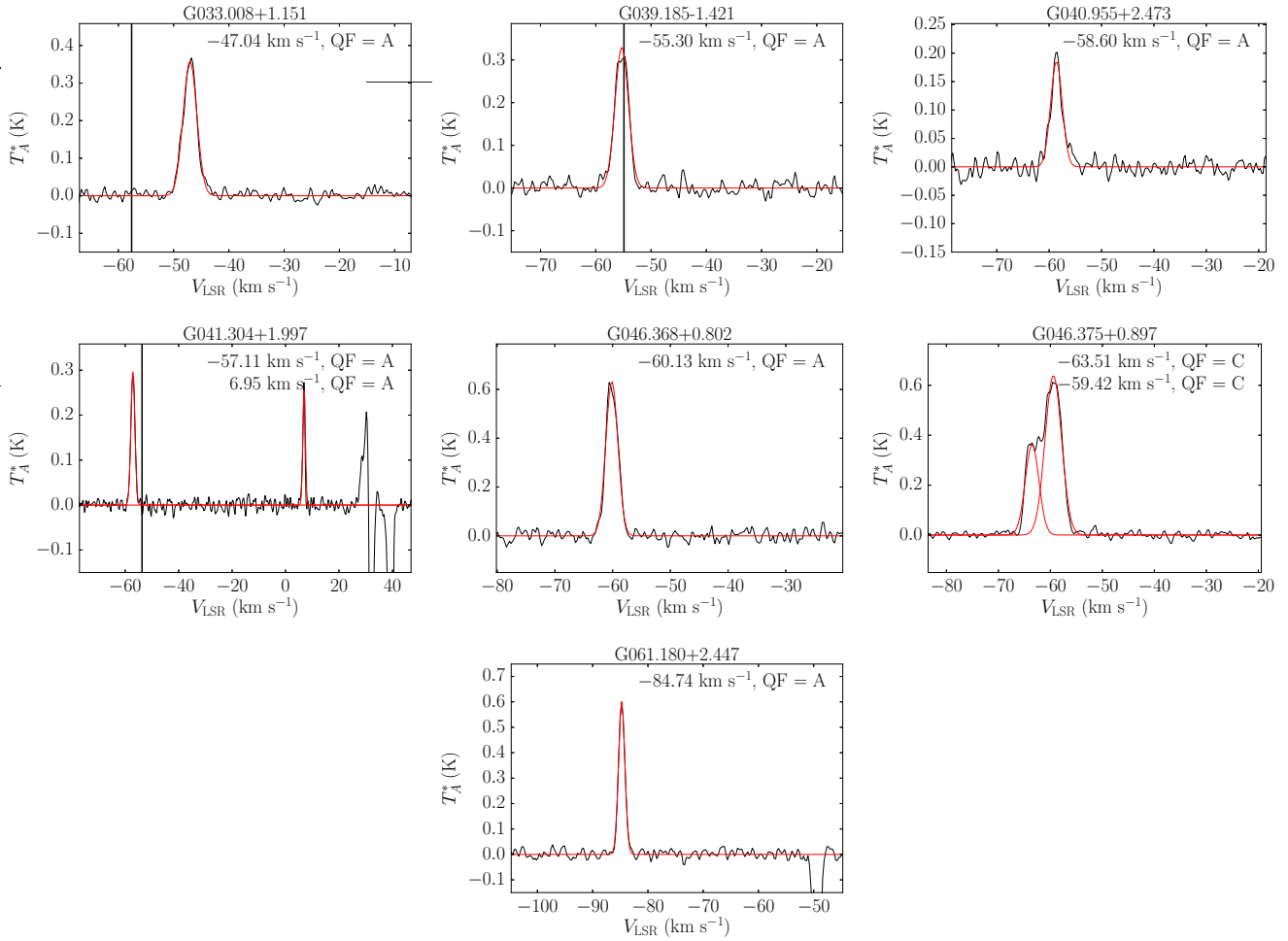


Figure 4. ^{13}CO spectra of emission lines originating within the OSC. Plotted is the antenna temperature as a function of the LSR velocity. The black curves are the data and the red curves are Gaussian fits to the data. The LSR velocity of each Gaussian profile, together with the QF, is shown in the right-hand corner of the plot. The vertical black line indicates the RRL velocity, when available.

remove any sky continuum emission or residual baseline structure in the spectrum. We fitted a Gaussian function to each profile using a Levenberg-Markwardt least squares method (Markwardt 2009) to derive the peak intensity, the full width at half-maximum (FWHM) line width, and the local standard of rest (LSR) velocity.

We compared the results of each independent analysis. The results were similar for $\sim 90\%$ of the spectra. Any differences typically involved how best to fit complex, blended profiles. Multiple ^{12}CO emission components were detected in about 2/3 of the targets. These directions thus contain several ^{12}CO clouds along the line-of-sight. Furthermore, because CO is pervasive in the inner Galactic plane, there was often ^{12}CO emission detected in the Off position. This creates apparent absorption lines in the processed position-switched spectrum. Since any emission components near these absorption features are contaminated by this Off emis-

sion, we eliminated these components from any further analysis. The ^{13}CO spectra were analyzed in the same manner.

We assigned a Quality Factor (A, B, or C) to every CO emission line. This judgment was based on the signal-to-noise ratio and expected line properties (e.g., the line widths should be a few km s^{-1} at most). A quality factor of “A” was given to profiles with a signal-to-noise ratio larger than 10 with no blending and flat spectral baselines. Targets with either lower signal-to-noise ratio or some blending of lines were given a quality factor “B”. Here the blending should not be so severe that the individual peaks could not be visually detected. A quality factor of “C” was given to the remaining targets which were often blended and more difficult to fit. A quality factor of D was assigned to spectra with no CO detections.

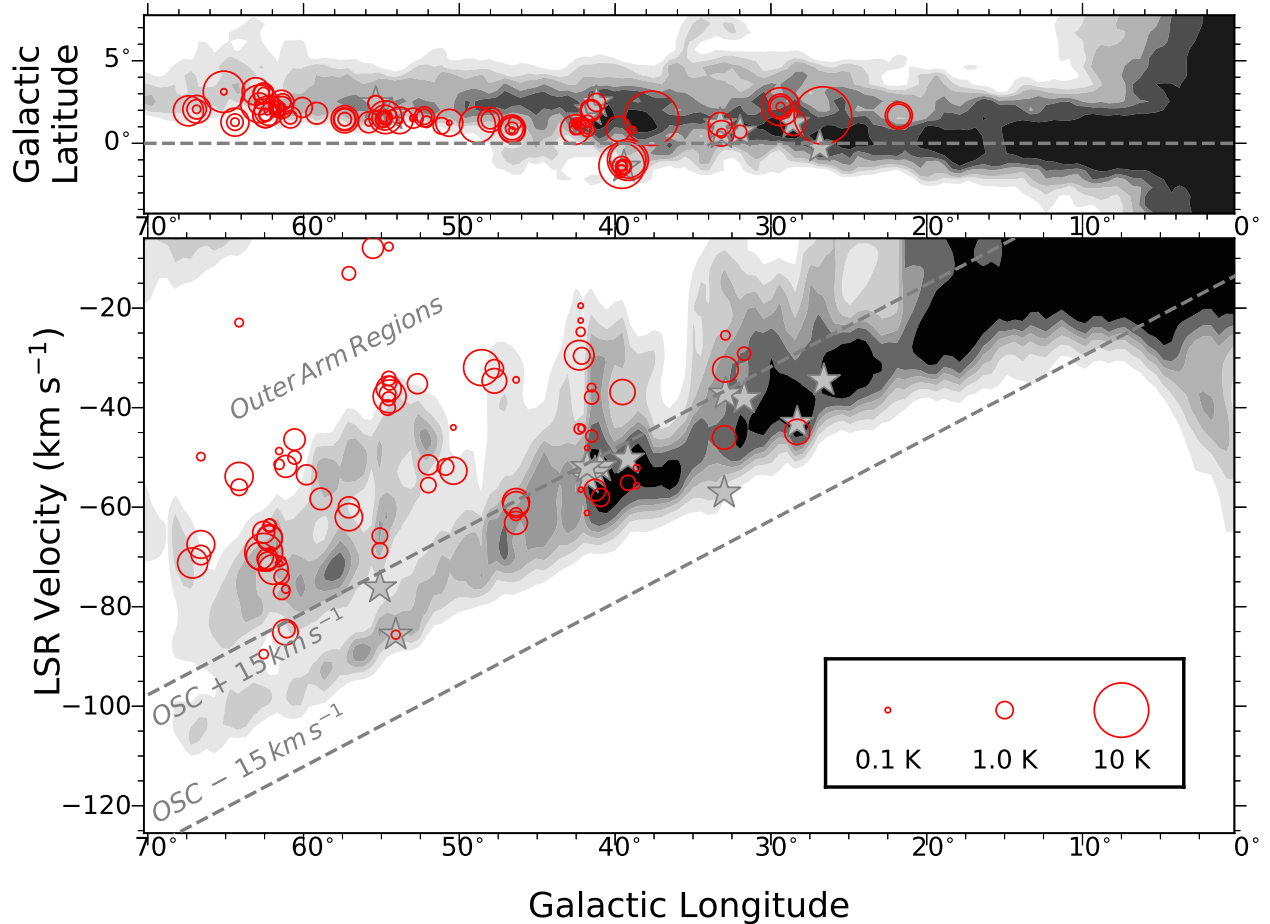


Figure 5. The outer Scutum-Centaurus spiral arm as traced by integrated H I emission, CO emission, and H II regions. Top: velocity-integrated H I emission (grayscale image) tracing the OSC spiral arm, summed over a 14 km s^{-1} wide window following the center velocity given by $V_{\text{LSR}} = -1.6 \text{ km s}^{-1} \text{ deg}^{-1} \times \ell$. CO emission detected here toward *WISE* H II regions is shown as red circles with sizes scaled by the ^{12}CO peak line intensity. Gray stars correspond to H II regions consistent with the location of the OSC (Armentrout et al. 2017). Bottom: longitude-velocity diagram of H I emission (grayscale image), summed over a 3.5 window following the arm in latitude with $b = 0.75 + 0.75 \times \ell$. The symbols are the same as in the top panel. The OSC locus is defined by $V_{\text{LSR}} = -1.6 \ell \pm 15 \text{ km s}^{-1}$ and shown by the dashed lines. (Reproduced from Dame & Thaddeus (2011) and Armentrout et al. (2017).)

3. RESULTS AND DISCUSSION

We detect CO toward $\sim 80\%$ of our targets. About 2/3 of our targets have at least one CO emission line at negative velocity, placing it beyond the Solar orbit. The results are summarized in Figures 1–4 and Tables 1–2. We measure 117 distinct ^{12}CO components toward 62 of 78 targets, and 40 ^{13}CO components toward 27 of 30 targets. Representative ^{12}CO spectra that span the range of quality factors A–C are shown in Figure 1. All line intensities are in units of the antenna temperature corrected for atmospheric attenuation, radiative loss, and rearward scattering and spillover, T_{A}^* . The Gaussian fit parameters are shown in Table 1 and Table 2 for the ^{12}CO and ^{13}CO spectra, respectively. Listed are

the target name, the Gaussian fit parameters, the root-mean-square noise in the line-free baseline, RMS, the total integration time, t_{intg} , and the quality factor, QF. The Gaussian fits include the peak line intensity, T_{L} , the LSR velocity, V_{LSR} , and the FWHM line width, ΔV , and their associated $1\text{-}\sigma$ uncertainties. For ^{12}CO spectra with multiple emission components, in Table 1 we append a letter at the end of the target name (a, b, c, etc.) in order of decreasing line intensity.

In most cases we can associate each ^{13}CO component with a corresponding ^{12}CO component using the LSR velocity (i.e. the ^{12}CO and ^{13}CO components have the same LSR velocity, within 2 km s^{-1}). There are four exceptions. In G050.901+1.056 and G062.194+1.715

there are two ^{13}CO components that correspond to one ^{12}CO component (identified as G050.901+1.056a, G050.901+1.056b, G062.194+1.715a1, and G062.194+1.715a2 in Table 2). The reverse occurs in G066.608+2.061 where there is one ^{13}CO component corresponding to two ^{12}CO components (identified as G066.608+2.061ab in Table 2). These differences may be caused by opacity effects where the ^{13}CO emission is arising from a region that is optically thick in ^{12}CO . This can cause self-absorption in the ^{12}CO spectrum. The signal-to-noise ratio will also affect the ability to resolve multiple components. Finally, for G061.154+2.170 there are ^{12}CO components at velocities where the ^{13}CO emission is corrupted by emission in the Off position. The ^{12}CO and ^{13}CO spectra for these four targets are shown in Figure 2.

Following Armentrout et al. (2017), we deem molecular emission components to be located in the OSC whenever the molecular line LSR velocity is within the (ℓ, v) locus defined by $V_{\text{LSR}} = -1.6\ell \pm 15 \text{ km s}^{-1}$. We find that 17 ^{12}CO emission lines toward 14 targets and 8 ^{13}CO emission lines toward 7 targets originate within the OSC. Of these detections, 7 ^{12}CO targets (G028.319+1.243, G033.008+1.151, G039.185-1.421, G041.304+1.997, G041.810+1.503, G054.094+1.749,

G062.578+2.387) and 3 ^{13}CO targets (G033.008+1.151, G039.185-1.421, G041.304+1.997) have a measured RRL velocity in the *WISE* Catalog of Galactic H II regions (Anderson et al. 2012). We show spectra for all of our OSC detections in Figure 3 and 4 for ^{12}CO and ^{13}CO , respectively. Two OSC targets have multiple ^{12}CO or ^{13}CO spectral line components that lie within the OSC: G038.627+0.813 and G046.375+0.897. Our OSC targets may not all be unique objects. There are two target pairs — G046.368+0.802/G046.375+0.897 and G061.085+2.502/G061.180+2.447 — that lie near the same (ℓ, b, v) locus and therefore may be part of the same star formation complex. This may account for the multiple component spectrum seen toward G046.375+0.897. Finally, six of our OSC targets are probably related to sources detected by Sun et al. (2017) in CO emission: G038.627+0.813ab (MWISP G38.533+0.892), G039.185-1.421 (MWISP G39.175-1.425), G040.955+2.473 (MWISP G40.958+2.483), G041.304+1.997 (MWISP G41.308+2.000), G041.810+1.503 (MWISP G41.758+1.567, MWISP G41.733+1.517, MWISP G41.742+1.458), and G042.210+1.081 (MWISP G42.192+1.083).

Table 1. ^{12}CO Emission Line Parameters

Name	T_L	σ_{T_L}	V_{LSR}	$\sigma_{V_{\text{LSR}}}$	ΔV	$\sigma_{\Delta V}$	RMS	t_{intg}	QF
	(K)	(K)	(km s^{-1})	(km s^{-1})	(km s^{-1})	(km s^{-1})	(K)	(min.)	
G021.541+1.676a	4.91	0.09	31.07	0.04	2.33	0.09	0.050	19.5	B
G021.541+1.676b	3.56	0.09	33.66	0.06	2.28	0.12	0.050	19.5	B
G023.610-0.212	0.034	39.0	D
G026.380+1.678	0.052	19.5	D
G026.418+1.683	22.30	0.17	43.32	0.02	4.49	0.04	0.031	38.9	A
G026.964+1.644	0.046	19.5	D
G028.319+1.243	4.32	0.04	-45.75	0.02	3.30	0.04	0.046	19.6	A
G029.136+2.219a	9.73	0.13	32.88	0.03	2.80	0.07	0.042	19.4	B
G029.136+2.219b	4.30	0.13	36.37	0.07	2.85	0.20	0.042	19.4	B
G029.136+2.219c	2.99	0.16	9.57	0.04	1.64	0.10	0.042	19.4	C
G029.136+2.219d	0.50	0.19	6.19	0.21	1.17	0.51	0.042	19.4	C
G031.727+0.698	1.16	0.03	-30.50	0.03	2.60	0.07	0.030	39.0	A
G032.928+0.606a	4.39	0.02	-33.55	0.01	3.89	0.03	0.043	19.5	B
G032.928+0.606b	0.58	0.02	-26.91	0.07	3.41	0.17	0.043	19.5	B
G033.008+1.151	3.75	0.05	-46.84	0.02	2.79	0.05	0.042	19.5	A
G034.172+1.055	0.039	19.5	D
G037.419+1.514	19.96	0.34	44.19	0.03	3.47	0.07	0.028	38.9	C
G038.627+0.813a	0.30	0.01	-52.76	0.05	2.55	0.13	0.028	38.9	B
G038.627+0.813b	0.24	0.01	-56.25	0.06	2.28	0.15	0.028	38.9	B
G038.931-1.003a	11.27	0.30	51.60	0.05	2.10	0.14	0.035	19.5	C

Table 1 continued

Table 1 (*continued*)

Name	T_L	σ_{T_L}	V_{LSR}	$\sigma_{V_{LSR}}$	ΔV	$\sigma_{\Delta V}$	RMS	t_{intg}	QF
	(K)	(K)	(km s^{-1})	(K)	(min.)				
G038.931-1.003b	8.83	0.71	49.93	0.06	1.74	0.07	0.035	19.5	C
G039.185-1.421a	1.52	0.01	-55.67	0.01	3.32	0.04	0.027	34.1	A
G039.185-1.421b	1.19	0.03	7.17	0.01	0.93	0.02	0.027	34.1	A
G039.328-1.350a	13.97	0.07	53.35	0.01	2.19	0.01	0.034	19.5	B
G039.328-1.350b	2.25	0.08	72.49	0.03	1.99	0.08	0.034	19.5	A
G039.328-1.350c	0.90	0.07	48.53	0.08	2.19	0.20	0.034	19.5	A
G039.328-1.350d	0.60	0.13	7.61	0.07	0.66	0.16	0.034	19.5	B
G039.342-1.676	0.92	0.02	56.17	0.02	1.56	0.04	0.034	19.5	A
G039.343-1.675	0.94	0.01	56.17	0.01	1.40	0.02	0.034	19.5	A
G039.536+0.873	4.25	0.08	-37.98	0.03	3.16	0.07	0.022	48.7	C
G039.823+1.977	0.034	19.5	D
G040.723+3.442	0.036	19.5	D
G040.955+2.473	2.22	0.05	-58.54	0.03	2.97	0.08	0.033	19.5	A
G041.304+1.997a	3.13	0.02	-57.09	0.01	2.16	0.02	0.039	19.5	A
G041.304+1.997b	2.49	0.03	6.87	0.01	1.25	0.02	0.039	19.5	A
G041.511+1.335	0.99	0.02	-46.57	0.02	1.71	0.04	0.032	38.9	A
G041.522+0.827a	1.32	0.02	-38.96	0.01	1.63	0.03	0.035	19.5	B
G041.522+0.827b	0.48	0.02	-37.10	0.03	1.09	0.06	0.035	19.5	B
G041.810+1.503a	0.19	0.01	-61.55	0.12	3.12	0.31	0.033	19.5	B
G041.810+1.503b	0.16	0.01	-48.87	0.11	3.54	0.26	0.033	19.5	B
G042.154+1.046a	1.86	0.04	-30.92	0.02	2.28	0.06	0.039	14.6	B
G042.154+1.046b	0.38	0.04	-45.03	0.12	2.31	0.30	0.039	14.6	A
G042.210+1.081	0.17	0.01	-57.02	0.10	2.74	0.23	0.025	39.0	B
G042.224+1.205a	0.54	0.02	-26.23	0.02	1.48	0.06	0.041	19.5	C
G042.224+1.205b	0.19	0.01	-21.14	0.07	1.73	0.16	0.041	19.5	C
G042.224+1.205c	0.18	0.02	-24.03	0.06	1.20	0.16	0.041	19.5	C
G042.311+0.831a	5.87	0.04	-30.79	0.01	2.68	0.02	0.029	29.2	A
G042.311+0.831b	0.72	0.04	-45.16	0.07	2.81	0.17	0.029	29.2	A
G044.122+2.570	0.036	38.9	D
G045.019+1.435	0.047	9.7	D
G045.161+2.331	0.034	19.5	D
G046.177+1.233	1.15	0.02	1.92	0.01	1.37	0.04	0.027	29.2	A
G046.368+0.802a	4.55	0.03	-59.92	0.01	2.40	0.02	0.034	19.5	A
G046.368+0.802b	0.26	0.04	-35.60	0.11	1.44	0.25	0.034	19.5	A
G046.375+0.897a	4.97	0.02	-59.44	0.02	3.90	0.04	0.030	38.9	C
G046.375+0.897b	3.49	0.04	-63.49	0.05	2.81	0.08	0.030	38.9	C
G046.375+0.897c	1.08	0.15	-61.79	0.04	1.42	0.13	0.030	38.9	C
G047.765+1.425a	4.07	0.04	-35.79	0.02	2.27	0.03	0.034	19.5	C
G047.765+1.425b	2.26	0.04	-33.43	0.04	2.44	0.06	0.034	19.5	C
G048.589+1.126	8.70	0.07	-33.21	0.01	2.98	0.03	0.024	39.0	C
G050.394+1.242a	4.92	0.05	-53.32	0.01	2.06	0.03	0.036	14.6	A
G050.394+1.242b	0.19	0.05	-44.88	0.28	2.10	0.67	0.036	14.6	B
G050.830+0.820	0.040	19.5	D
G050.901+1.056	1.83	0.03	-52.58	0.02	2.67	0.05	0.023	39.0	A
G050.901+2.554	0.022	39.0	D
G051.854+1.305	0.89	0.02	58.37	0.02	2.28	0.05	0.041	19.4	A
G052.002+1.602a	2.70	0.05	-52.17	0.02	2.52	0.06	0.036	14.6	B
G052.002+1.602b	1.57	0.05	-56.12	0.04	2.44	0.10	0.036	14.6	B

Table 1 *continued*

Table 1 (*continued*)

Name	T_L	σ_{T_L}	V_{LSR}	$\sigma_{V_{LSR}}$	ΔV	$\sigma_{\Delta V}$	RMS	t_{intg}	QF
	(K)	(K)	(km s^{-1})	(K)	(min.)				
G052.021+1.629	0.039	19.5	D
G052.073+2.737	0.022	38.9	D
G052.706+1.526a	2.69	0.03	-36.36	0.01	1.71	0.02	0.031	19.5	A
G052.706+1.526b	0.33	0.04	7.10	0.06	0.96	0.14	0.031	19.5	B
G052.706+1.526c	0.22	0.04	5.62	0.08	0.88	0.21	0.031	19.5	B
G053.334+0.895	0.032	19.5	D
G053.396+3.060	0.033	19.5	D
G053.449+0.871	0.033	19.5	D
G053.581+1.388a	4.75	0.02	43.96	0.00	1.35	0.01	0.033	19.5	A
G053.581+1.388b	0.25	0.02	50.70	0.06	1.41	0.13	0.033	19.5	A
G054.094+1.749	0.52	0.01	-85.29	0.02	1.83	0.05	0.021	38.9	A
G054.491+1.579a	7.28	0.06	-38.82	0.01	2.37	0.03	0.021	39.0	C
G054.491+1.579b	1.26	0.08	-36.25	0.05	1.30	0.11	0.021	39.0	C
G054.544+1.559a	4.20	0.03	-37.29	0.06	3.45	0.10	0.023	39.0	C
G054.544+1.559b	1.36	0.12	-35.32	0.02	1.67	0.08	0.023	39.0	C
G054.544+1.559c	1.24	0.13	-39.27	0.02	1.61	0.10	0.023	39.0	C
G054.544+1.559d	0.50	0.02	-9.61	0.03	1.39	0.06	0.023	39.0	A
G054.616+1.452a	1.84	0.04	-38.27	0.02	1.50	0.04	0.033	19.5	B
G054.616+1.452b	1.58	0.04	-41.00	0.02	1.85	0.07	0.033	19.5	B
G055.114+2.420a	1.62	0.04	-66.00	0.10	3.38	0.15	0.030	19.5	C
G055.114+2.420b	1.61	0.07	-68.91	0.08	2.75	0.11	0.030	19.5	C
G055.560+1.272a	2.96	0.21	-9.86	0.06	1.63	0.13	0.033	19.5	A
G055.560+1.272b	0.38	0.14	44.42	0.74	4.16	1.89	0.033	19.5	A
G057.107+1.457a	4.99	0.25	-62.38	0.16	2.67	0.25	0.023	38.9	C
G057.107+1.457b	3.51	0.14	33.51	0.03	1.65	0.07	0.023	38.9	B
G057.107+1.457c	2.98	0.65	-60.46	0.14	1.81	0.21	0.023	38.9	A
G057.107+1.457d	1.21	0.12	-14.83	0.10	1.94	0.23	0.023	38.9	C
G058.903+1.820	3.14	0.04	-58.81	0.01	1.52	0.02	0.036	14.6	A
G058.988+1.469	0.024	38.9	D
G059.829+2.171	2.68	0.05	-54.11	0.02	1.64	0.04	0.040	19.5	A
G060.595+1.572a	3.05	0.12	-47.24	0.08	2.71	0.14	0.043	9.7	C
G060.595+1.572b	1.19	0.07	-50.74	0.26	3.71	0.52	0.043	9.7	C
G061.085+2.502	1.81	0.05	-84.29	0.02	1.66	0.05	0.031	19.5	A
G061.154+2.170a	3.23	0.31	-52.47	0.11	2.25	0.25	0.035	19.4	A
G061.154+2.170b	0.44	0.40	-76.40	0.62	1.38	1.46	0.035	19.4	A
G061.154+2.170c	0.33	0.28	36.10	1.19	2.94	2.81	0.035	19.4	A
G061.180+2.447	4.31	0.04	-84.81	0.01	1.71	0.02	0.031	19.5	A
G061.424+2.076a	1.80	0.02	-76.84	0.04	3.45	0.09	0.030	19.5	B
G061.424+2.076b	1.54	0.05	-73.99	0.03	2.08	0.08	0.030	19.5	B
G061.424+2.076c	0.52	0.02	-70.94	0.09	2.97	0.21	0.030	19.5	B
G061.587+2.074a	0.69	0.02	-52.07	0.02	1.53	0.05	0.031	19.5	A
G061.587+2.074b	0.47	0.02	26.21	0.03	1.21	0.07	0.031	19.5	A
G061.587+2.074c	0.33	0.02	-49.48	0.04	1.11	0.09	0.031	19.5	B
G061.587+2.074d	0.31	0.02	-71.40	0.06	1.93	0.13	0.031	19.5	B
G061.955+1.983	5.90	0.04	-72.57	0.01	2.90	0.02	0.033	19.5	A
G062.075+1.901	0.24	0.02	-68.75	0.08	2.44	0.19	0.033	19.5	A
G062.194+1.715a	4.27	0.07	-66.29	0.04	2.61	0.09	0.031	19.5	C
G062.194+1.715b	1.21	0.13	-64.01	0.08	1.39	0.17	0.031	19.5	C

Table 1 *continued*

Table 1 (continued)

Name	T_L	σ_{T_L}	V_{LSR}	$\sigma_{V_{\text{LSR}}}$	ΔV	$\sigma_{\Delta V}$	RMS	t_{intg}	QF
	(K)	(K)	(km s ⁻¹)	(km s ⁻¹)	(km s ⁻¹)	(km s ⁻¹)	(K)	(min.)	
G062.197+1.715a	4.37	0.05	-66.50	0.02	2.82	0.05	0.023	38.9	C
G062.197+1.715b	0.95	0.07	-63.95	0.06	1.44	0.14	0.023	38.9	C
G062.325+3.020a	2.95	0.06	-70.49	0.01	2.96	0.03	0.032	19.4	C
G062.325+3.020b	2.50	0.06	-71.03	0.01	1.20	0.02	0.032	19.4	C
G062.325+3.020c	0.95	0.02	7.79	0.02	1.62	0.04	0.032	19.4	A
G062.578+2.387a	9.56	0.03	-69.20	0.01	3.76	0.03	0.023	38.9	C
G062.578+2.387b	3.21	0.05	-65.33	0.04	2.99	0.07	0.023	38.9	A
G062.578+2.387c	0.57	0.06	-89.09	0.06	1.29	0.16	0.023	38.9	C
G062.819+3.144	5.03	0.04	-69.92	0.01	1.40	0.01	0.034	19.5	A
G064.151+1.282a	5.30	0.08	-54.42	0.04	2.95	0.05	0.023	38.9	C
G064.151+1.282b	1.83	0.15	-56.54	0.07	2.33	0.08	0.023	38.9	C
G064.151+1.282c	0.48	0.02	-24.43	0.05	2.33	0.11	0.023	38.9	A
G064.862+3.120a	11.50	0.07	-1.79	0.01	1.99	0.01	0.031	19.5	A
G064.862+3.120b	0.26	0.07	26.67	0.28	2.22	0.65	0.031	19.5	A
G066.608+2.061a	5.16	0.39	-67.69	0.09	2.55	0.08	0.031	19.5	C
G066.608+2.061b	2.54	0.30	-69.76	0.22	2.77	0.24	0.031	19.5	C
G066.608+2.061c	0.46	0.04	-50.57	0.08	1.97	0.19	0.031	19.5	A
G067.138+1.966	6.10	0.11	-71.31	0.02	1.80	0.04	0.024	38.9	C

NOTE—Names in bold face have V_{LSR} within OSC velocity range defined by $V_{\text{LSR}} = -1.6\ell \pm 15 \text{ km s}^{-1}$.

3.1. CO Distribution throughout the Milky Way

How are the molecular clouds with detected CO emission distributed in the Galaxy? Our targets were selected from the *WISE* H II region catalog and therefore their distribution should reflect the Galactic H II region or high-mass star formation distribution. We expect that in many cases the CO emission is associated with the H II region along the line-of-sight, but this is not always true (Russeil & Castets 2004; Anderson et al. 2009).

The most direct view is given by the observed, model independent, parameters: ℓ, b, v . Figure 5 shows the (ℓ, b) (top) and the (ℓ, v) diagrams (bottom) for the OSC region of the Galaxy. Similar plots are found in Dame & Thaddeus (2011) and Armentrout et al. (2017). Integrated HI emission is shown together with

our ¹²CO detections (red circles). The molecular clouds trace the warp in the disk as defined by HI emission but are concentrated at the lower latitude end of the HI envelope. The bottom panel of Figure 5 shows the molecular clouds located in the OSC as red circles between the dashed lines. Several of these are clearly associated with H II regions indicated by the gray stars.

Since the majority of our targets have multiple emission components, we cannot identify which CO component might be associated with the H II region. Nevertheless, most of the molecular clouds in our sample have negative velocities and are thus located beyond the Solar orbit. In fact, Figure 5 shows that the majority of the negative velocity components CO seem to be located in the Outer Arm and not the more-distant OSC.

Table 2. ¹³CO Emission Line Parameters

Name	T_L	σ_{T_L}	V_{LSR}	$\sigma_{V_{\text{LSR}}}$	ΔV	$\sigma_{\Delta V}$	RMS	t_{intg}	QF
	(K)	(K)	(km s ⁻¹)	(km s ⁻¹)	(km s ⁻¹)	(km s ⁻¹)	(K)	(min.)	
G033.008+1.151	0.36	0.01	-47.04	0.03	2.93	0.06	0.010	77.9	A
G038.627+0.813	0.011	68.2	D
G039.185-1.421a	0.33	0.01	-55.30	0.03	2.87	0.08	0.012	58.4	A
G040.955+2.473	0.19	0.01	-58.60	0.05	2.62	0.12	0.011	63.3	A
G041.304+1.997a	0.30	0.01	-57.11	0.02	1.77	0.04	0.011	58.4	A

Table 2 continued

Table 2 (*continued*)

Name	T_L (K)	σ_{T_L} (K)	V_{LSR} (km s^{-1})	$\sigma_{V_{LSR}}$ (km s^{-1})	ΔV (km s^{-1})	$\sigma_{\Delta V}$ (km s^{-1})	RMS (K)	t_{intg} (min.)	QF
G041.304+1.997b	0.26	0.01	6.95	0.04	1.14	0.08	0.011	58.4	A
G041.511+1.335	0.15	0.00	-46.67	0.02	1.23	0.05	0.011	58.4	A
G046.368+0.802a	0.63	0.01	-60.13	0.03	2.46	0.06	0.021	19.5	A
G046.375+0.897a	0.64	0.01	-59.42	0.07	3.73	0.14	0.011	68.1	C
G046.375+0.897b	0.36	0.01	-63.51	0.10	3.09	0.22	0.011	68.1	C
G050.394+1.242a	0.61	0.01	-53.55	0.01	1.81	0.02	0.020	19.5	A
G050.901+1.056a	0.26	0.01	-51.89	0.04	1.32	0.07	0.011	58.4	C
G050.901+1.056b	0.12	0.01	-53.37	0.13	1.71	0.23	0.011	58.4	C
G052.002+1.602a	0.34	0.01	-52.56	0.03	2.17	0.08	0.011	58.4	B
G052.002+1.602b	0.17	0.01	-55.81	0.07	2.18	0.21	0.011	58.4	B
G054.094+1.749	0.009	77.9	D
G055.114+2.420b	0.12	0.01	-68.67	0.04	1.34	0.11	0.011	58.4	C
G055.114+2.420a	0.11	0.01	-67.62	0.11	4.64	0.19	0.011	58.4	C
G057.107+1.457a	1.35	0.02	-61.67	0.02	2.58	0.04	0.019	19.5	A
G058.903+1.820	0.36	0.02	-58.78	0.03	1.26	0.07	0.012	48.7	A
G059.829+2.171	0.75	0.01	-54.17	0.01	1.26	0.02	0.015	24.3	A
G060.595+1.572a	0.28	0.01	-47.45	0.03	1.50	0.08	0.012	48.7	C
G060.595+1.572b	0.14	0.01	-48.61	0.15	6.56	0.33	0.012	48.7	C
G061.154+2.170a	0.82	0.01	-52.44	0.01	1.80	0.03	0.016	19.6	A
G061.154+2.170d	0.53	0.01	11.67	0.05	2.39	0.11	0.016	19.6	A
G061.154+2.170e	0.22	0.02	4.58	0.04	1.06	0.09	0.016	19.6	A
G061.180+2.447	0.60	0.01	-84.74	0.01	1.35	0.02	0.017	19.5	A
G061.424+2.076a	0.40	0.05	-76.59	0.21	2.57	0.26	0.017	19.4	C
G061.424+2.076b	0.24	0.04	-74.24	0.39	2.76	0.49	0.017	19.4	C
G061.955+1.983	1.23	0.01	-72.64	0.01	2.34	0.03	0.017	19.5	A
G062.075+1.901	0.010	58.4	D
G062.194+1.715a1	0.44	0.03	-66.09	0.03	1.26	0.07	0.010	58.3	C
G062.194+1.715a2	0.24	0.01	-67.49	0.08	1.80	0.13	0.010	58.3	C
G062.194+1.715b	0.21	0.01	-64.66	0.09	1.86	0.13	0.010	58.3	C
G062.197+1.715a	0.80	0.02	-66.09	0.04	2.78	0.09	0.017	19.4	A
G062.325+3.020b	1.15	0.04	-70.78	0.03	1.23	0.04	0.018	19.5	C
G062.325+3.020a	0.57	0.03	-69.61	0.07	1.37	0.09	0.018	19.5	C
G062.578+2.387a	1.88	0.01	-69.28	0.01	3.04	0.03	0.018	19.5	C
G062.578+2.387b	0.46	0.01	-65.55	0.04	2.52	0.10	0.018	19.5	C
G062.819+3.144	0.68	0.01	-69.84	0.01	1.25	0.02	0.017	19.4	A
G064.151+1.282a	0.64	0.01	-54.88	0.02	2.91	0.05	0.016	19.5	A
G066.608+2.061ab	1.60	0.04	-68.21	0.03	2.42	0.08	0.017	19.5	A
G067.138+1.966	1.26	0.01	-71.47	0.01	1.37	0.02	0.017	19.5	A

NOTE—Names in bold face have V_{LSR} within OSC velocity range defined by $V_{LSR} = -1.6\ell \pm 15 \text{ km s}^{-1}$.

Table 3. Molecular Cloud Properties

Name	V_{LSR} (km s^{-1})	R_{gal} (kpc)	d_{\odot} (kpc)	$T_L(^{12}\text{CO})$ (K)	$T_L(^{13}\text{CO})$ (K)	$N(\text{H}_2)$ (10^{20} cm^{-2})
G033.008+1.151	-46.84	14.44	20.81	3.75	0.36	5.19
G039.185-1.421a	-55.67	14.69	20.26	1.52	0.33	4.66

Table 3 continued

Table 3 (*continued*)

Name	V_{LSR} (km s^{-1})	R_{gal} (kpc)	d_{\odot} (kpc)	$T_{\text{L}}(^{12}\text{CO})$ (K)	$T_{\text{L}}(^{13}\text{CO})$ (K)	$N(\text{H}_2)$ (10^{20} cm^{-2})
G040.955+2.473	-58.54	14.83	20.16	2.22	0.19	2.45
G041.304+1.997a	-57.09	14.50	19.76	3.13	0.30	2.61
G041.304+1.997b	6.87	8.22	0.38/12.39	2.49	0.26	1.46
G041.511+1.335	-46.57	12.87	17.94	0.99	0.15	0.91
G046.368+0.802a	-59.92	14.09	18.55	4.55	0.63	7.63
G046.375+0.897a	-59.44	14.02	18.46	4.97	0.64	11.75
G046.375+0.897b	-63.49	14.64	19.14	3.49	0.36	5.47
G050.394+1.242a	-53.32	12.78	16.39	4.92	0.61	5.43
G050.901+1.056a	-52.58	12.65	16.16	1.83	0.26	1.69
G050.901+1.056b	-52.58	12.65	16.16	1.83	0.12	1.01
G052.002+1.602a	-52.17	12.52	15.81	2.70	0.34	3.63
G052.002+1.602b	-56.12	12.96	16.32	1.57	0.17	1.82
G055.114+2.420a	-66.00	13.86	16.84	1.62	0.11	2.51
G055.114+2.420b	-68.91	14.23	17.27	1.61	0.12	0.79
G057.107+1.457a	-62.38	13.24	15.77	4.99	1.35	17.14
G058.903+1.820	-58.81	12.73	14.84	3.14	0.36	2.23
G059.829+2.171	-54.11	12.22	14.04	2.68	0.75	4.65
G060.595+1.572a	-47.24	11.58	13.08	3.05	0.28	2.07
G060.595+1.572b	-50.74	11.88	13.46	1.19	0.14	4.52
G061.154+2.170a	-52.47	12.01	13.52	3.23	0.82	7.26
G061.180+2.447	-84.81	15.77	18.00	4.31	0.60	3.99
G061.424+2.076a	-76.84	14.62	16.64	1.80	0.40	5.06
G061.424+2.076b	-73.99	14.25	16.21	1.54	0.24	3.26
G061.955+1.983	-72.57	14.04	15.86	5.90	1.23	14.16
G062.194+1.715a1	-66.29	13.30	14.94	4.27	0.44	2.73
G062.194+1.715a2	-66.29	13.30	14.94	4.27	0.24	2.13
G062.194+1.715b	-64.01	13.06	14.64	1.21	0.21	1.92
G062.197+1.715a	-66.50	13.33	14.97	4.37	0.80	10.94
G062.325+3.020a	-70.49	13.77	15.48	2.95	0.57	3.84
G062.325+3.020b	-71.03	13.83	15.55	2.50	1.15	6.96
G062.578+2.387a	-69.20	13.60	15.23	9.56	1.88	28.12
G062.578+2.387b	-65.33	13.18	14.72	3.21	0.46	5.70
G062.819+3.144	-69.92	13.67	15.27	5.03	0.68	4.18
G064.151+1.282a	-54.42	12.05	13.02	5.30	0.64	9.16
G067.138+1.966	-71.31	13.54	14.35	6.10	1.26	8.49

NOTE—Sources within the Solar circle have two values for the Distance (d_{\odot}) since we did not resolve the kinematic distance ambiguity.

Face-on maps of the Milky Way disk are difficult to make since distances to the sources are required. Parallax distances are the most accurate but can only be measured for a relatively small sample (e.g., see Reid et al. 2014). Kinematic distances are far easier to derive since they only require a spectral line velocity and a model of Galactic rotation. The main limitations are that the rotation curves suffer from non-circular (streaming) motions, and that within the Solar orbit there is a kinematic distance ambiguity (e.g., Anderson et al. 2012). Studies of the OSC arm avoid the latter problem be-

cause the OSC is located beyond the Solar orbit and so does not suffer from the distance ambiguity issue.

We use the Brand & Blitz (1993) rotation curve to determine kinematic distances to H I and CO emission as well as H II regions. The resulting face-on map for the first quadrant OSC zone studied here is shown in Figure 6 where the gray crosses are taken from the WISE H II region catalog and the red circles are CO emission from this study. We also include previously detected OSC H II regions (gray stars) and H I data (gray contours). The H II regions and molecular clouds associated with the OSC span a wide range of longitudes in the first

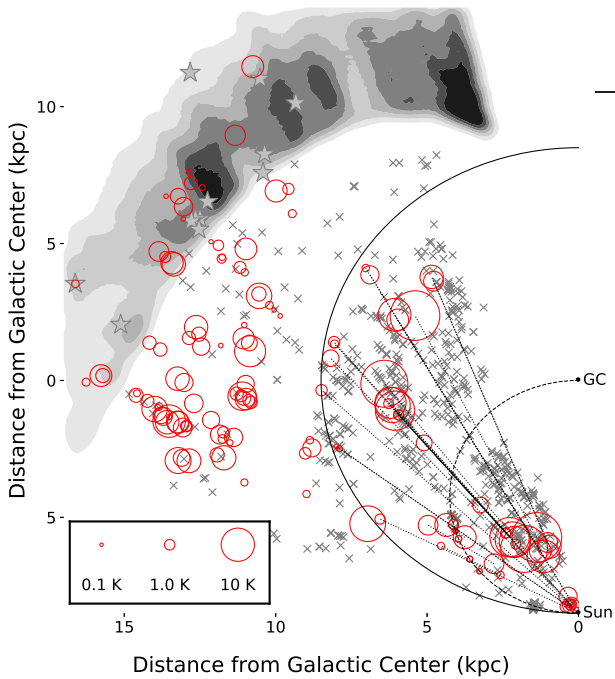


Figure 6. Face-on map of H II regions, CO emission components, and HI emission in the first Galactic quadrant. Plotted are H II regions from the *WISE* H II region catalog (gray crosses), H II regions consistent with the location of the OSC (gray stars), and CO emission detected here in the direction of *WISE* H II regions (red circles). The red circle sizes are scaled by the intensity of the ^{12}CO peak line intensity. The Solar circle and tangent points are indicated by the solid and dashed curves, respectively. The dotted lines connect the near and far kinematic distances for sources within the Solar orbit since we did not resolve the kinematic distance ambiguity. The gray scale shows OSC HI emission from the LAB survey. Here the OSC is defined in latitude and velocity as: $V_{\text{LSR}} = -1.6 \text{ km s}^{-1} \text{ deg}^{-1} \times \ell$ and $b = 0^\circ.75 + 0.75 \times \ell$. This is the same HI emission shown between the dashed lines in Figure 5 (bottom panel), but transformed using the Brand rotation curve (Brand & Blitz 1993). (Reproduced from Armentrout et al. (2017).)

Galactic quadrant. Their distribution is well-matched to the OSC extent delineated by HI emission.

3.2. Comparison of OSC and non-OSC CO Clouds

We search for differences between the emission line properties of molecular clouds in the OSC and clouds not in the OSC. Figure 7 shows the ^{12}CO and ^{13}CO FWHM line widths as a function of Galactocentric radius, R . The ratio of the mean ^{12}CO FWHM line width of OSC clouds to non-OSC clouds is 1.13 with a standard deviation of 0.52. For ^{13}CO the ratio is 1.23 with a standard deviation of 0.74. This evidence suggests

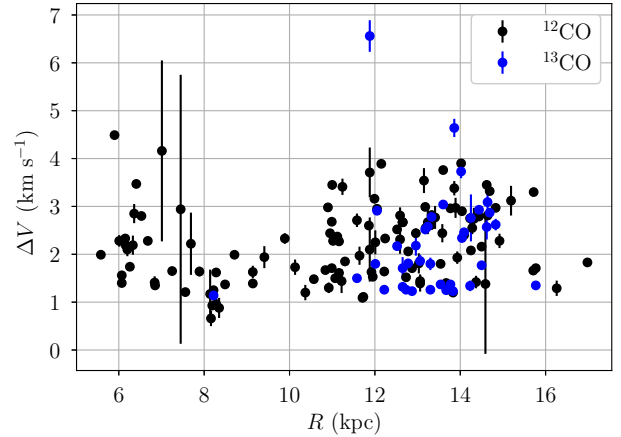


Figure 7. ^{12}CO (black) and ^{13}CO (blue) emission line FWHM line width, ΔV , as a function of Galactocentric radius, R . The black circles and black squares are the ^{12}CO and ^{13}CO FWHM line widths, respectively. The error bars are the 1σ uncertainties in the measured FWHM line widths.

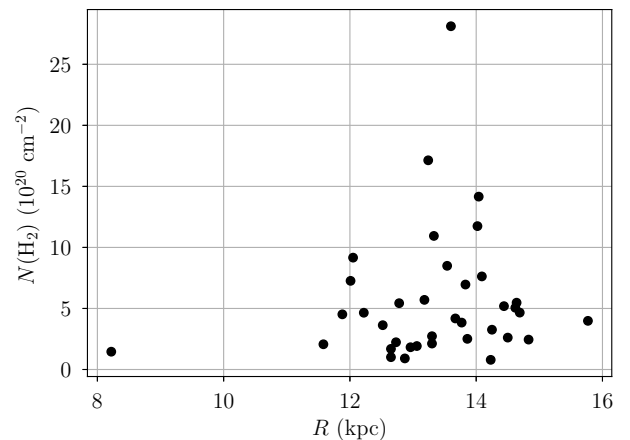


Figure 8. Molecular column density, $N(\text{H}_2)$, as a function of Galactocentric radius, R , for molecular clouds with ^{13}CO detections.

molecular cloud velocity dispersions are fairly uniform for all molecular clouds in our sample. We note, however, that our observations are a single pointing in the direction of the cloud rather than a full map. Our derived FWHM line widths are therefore likely lower limits of the true molecular cloud FWHM line widths, especially if the clouds are much larger than our beam ($\sim 1'$).

The ^{13}CO emission lines should be optically thin and may be used to derive the total molecular column densities of the molecular clouds. We derive the total H_2 column density of each of our ^{13}CO detections using Equation (2) from Simon et al. (2001). This equation

assumes a $^{12}\text{CO}/^{13}\text{CO}$ abundance ratio of 45, an excitation temperature of 10 K, and an X-factor ($^{12}\text{CO}/\text{H}_2$) of 8×10^{-5} . We assume the main beam efficiency is near unity and use the ^{13}CO emission line properties from Table 2. The molecular cloud column densities are compiled in Table 3 where we list the ^{12}CO component name, the LSR velocity, the Galactocentric radius, the distance from the Sun, the ^{12}CO and ^{13}CO line intensities, and the molecular column density. Sources within the Solar circle have two values for the distance since we did not resolve the kinematic distance ambiguity.

The total molecular column density of these clouds also does not have any trend with R . Figure 8 shows the derived H_2 column densities as a function of R for each of our clouds with ^{13}CO detections. The ratio of the mean molecular column densities of OSC clouds to non-OSC clouds is 0.97 with a standard deviation of 1.11. This evidence again suggests no difference between OSC and non-OSC molecular clouds within our sample with the caveat that our pointed observations likely underestimate the true molecular cloud FWHM line widths, and therefore these derived column densities may represent lower limits.

Since we expect molecular clouds to be extended in CO emission and have not mapped these regions, we cannot accurately derive the total molecular mass of these complexes. The eight sources from the MWISP survey in common with our survey have molecular masses and radii that range from $\sim 200 - 7000 M_\odot$ and $\sim 3 - 13$ pc, respectively. Since the molecular masses were calculated using ^{12}CO intensities that are likely optically thick, these should be interpreted as lower limits.

4. CONCLUSION

The Outer Scutum-Centaurus (OSC) spiral arm is the most distant site of massive star formation in the Milky Way. The OSC contains at least 12 known H II regions

ionized by high-mass stars with spectral types as early as O4. Molecular clouds have been detected within the OSC but most have not been associated with H II regions. Here we use the Arizona Radio Observatory (ARO) 12 m telescope to observe CO emission from 78 *WISE* H II region candidates located within the Galactic longitude-latitude (ℓ, b) locus of the OSC spiral arm in the first quadrant ($20^\circ < \ell < 90^\circ$). We detect 117 ^{12}CO spectral line components in 62 of 78 targets, and 40 ^{13}CO components in 27 of 30 targets. About 2/3 of the molecular clouds reside beyond the Solar orbit and are associated with the Outer Arm. We discovered 17 ^{12}CO emission lines and 8 ^{13}CO emission lines consistent with the (ℓ, v) OSC locus. These OSC molecular clouds have the same physical properties (FWHM line widths and molecular column densities) as non-OSC clouds within our sample.

We thank T. M. Dame and the anonymous referee for their useful comments and suggestions which improved the quality of this paper. T.V.W. is supported by the NSF through the Grote Reber Fellowship Program administered by Associated Universities, Inc./National Radio Astronomy Observatory, the D.N. Batten Foundation Fellowship from the Jefferson Scholars Foundation, the Mars Foundation Fellowship from the Achievement Rewards for College Scientists Foundation, and the Virginia Space Grant Consortium. L.D.A. is supported by NSF grant AST1516021. The Kitt Peak 12 Meter is operated by the Arizona Radio Observatory (ARO), Steward Observatory, University of Arizona. The National Radio Astronomy Observatory is a facility of the National Science Foundation operated under cooperative agreement by Associated Universities, Inc.

Facilities: ARO 12 m

Software: TMBIDL (Bania et al. 2016)

REFERENCES

- Anderson, L. D., Armentrout, W. P., Johnstone, B. M., et al. 2015, *ApJS*, 221, 26
- Anderson, L. D., Bania, T. M., Balser, D. S., & Rood, R. T. 2012, *ApJ*, 754, 62
- Anderson, L. D., Bania, T. M., Jackson, J. M., et al. 2009, *ApJS*, 181, 255
- Armentrout, W. P., Anderson, L. D., Balser, D. S., et al. 2017, *ApJ*, 841, 121
- Arnal, E. M., Bajaja, E., Larrarte, J. J., Morras, R., & Pöppel, W. G. L. 2000, *A&AS*, 142, 35
- Bajaja, E., Arnal, E. M., Larrarte, J. J., et al. 2005, *A&A*, 440, 767
- Bania, T., Wenger, T., Balser, D., & Anderson, L. 2016, TMBIDL: Single dish radio astronomy data reduction package, Astrophysics Source Code Library, , , ascl:1605.005
- Brand, J., & Blitz, L. 1993, *A&A*, 275, 67
- Churchwell, E., Babler, B. L., Meade, M. R., et al. 2009, *PASP*, 121, 213
- Dame, T. M., & Thaddeus, P. 2011, *ApJL*, 734, L24

- Elmegreen, D. M., & Elmegreen, B. G. 1982, MNRAS, 201, 1021
- Hartmann, D., & Burton, W. B. 1997, Atlas of Galactic Neutral Hydrogen (Cambridge University Press), 243
- Kalberla, P. M. W., Burton, W. B., Hartmann, D., et al. 2005, A&A, 440, 775
- Kerr, F. J. 1969, ARA&A, 7, 39
- Koo, B.-C., Park, G., Kim, W.-T., et al. 2017, PASP, 129, 094102
- Markwardt, C. B. 2009, in Astronomical Society of the Pacific Conference Series, Vol. 411, Astronomical Data Analysis Software and Systems XVIII, ed. D. A. Bohlender, D. Durand, & P. Dowler, 251
- Reid, M. J., Menten, K. M., Brunthaler, A., et al. 2014, ApJ, 783, 130
- Russeil, D., & Castets, A. 2004, A&A, 417, 107
- Simon, R., Jackson, J. M., Clemens, D. P., Bania, T. M., & Heyer, M. H. 2001, ApJ, 551, 747
- Sun, Y., Su, Y., Zhang, S.-B., et al. 2017, ApJS, 230, 17
- Sun, Y., Xu, Y., Yang, J., et al. 2015, ApJL, 798, L27
- Weaver, H. 1974, in IAU Symposium, Vol. 60, Galactic Radio Astronomy, ed. F. J. Kerr & S. C. Simonson, 573